Supplementary Information

Reconfigurable Ambipolar Non-Volatile Transistors for Fuzzy Logic-Enabled Edge Computing

Miao Zhang[a,c], Xingrou Meng[a,c], Haoxiang Tian[a], Weiming Pu[a], Houze Huang[a], Keqin Liu[a], Long Chen[a,b], Gaofeng Rao*[a], Xianfu Wang*[a]*

[a] State Key Laboratory of Electronic Thin Film and Integrated Devices, University of Electronic Science and Technology of China, Chengdu, China

[b] Yangtze Region Institute (Quzhou), University of Electronic Science and Technology of China, Quzhou, 324003, China.

[c] These authors contributed equally.

Experimental Section

Device fabrication: CIPS, hBN, and Black Phosphorus (BP) crystals were purchased from HQ-graphene and mechanically exfoliated into flakes on Polydimethylsiloxane (PDMS) or silicon substrates1. Highly doped silicon wafers with a 20 nm HfO_2 layer deposited by Atomic Layer Deposition (ALD) were used as the back-gate substrate to ensure low leakage current. The BP channel was transferred onto the HfO_2 substrate using a dry transfer method. Standard electron-beam lithography (EBL) and thermal evaporation were employed to pattern the source and drain electrodes (Cr/Au, 5/25 nm). To achieve n-type doping and protect the BP channel, a 2 nm Al_2O_3 layer was deposited via ALD. Subsequently, the hBN tunneling layer and CIPS ferroelectric flake were sequentially transferred onto the channel to form the CIPS/hBN/BP/ HfO_2 heterostructure. Finally, the top-gate electrodes (Cr/Au, 5/50 nm) were fabricated using EBL and evaporation processes.

Electrical measurements: The electrical performance of the devices was characterized using a vacuum probe station (Lake Shore, typically < 10^{-5} Torr) to prevent the degradation of BP in the ambient atmosphere. Data acquisition was performed using a semiconductor device parameter analyzer (Keithley 4200A-SCS). Raman spectra were collected using a confocal Raman microscope (Renishaw inVia) with a 532 nm excitation laser to verify the material quality and heterostructure integrity.

Supplementary Note 1: Algorithm principle and mathematical model of the embedded fuzzy logic layer

Precise edge detection and boundary delineation are paramount in medical diagnostics, where the ambiguity between lesion and normal tissue often limits the performance of conventional networks[1-4]. To computationally emulate the ambipolar transfer characteristics of the Al_2O_3-encapsulated BP reconfigurable transistor, we designed a differentiable Fuzzy Logic Layer integrated within the Convolutional Neural Network (CNN). This layer is mathematically abstracted from the device's physical ability to modulate current in a Gaussian-like manner (as shown in Figure 2c of the main text).

To evaluate the performance of our proposed network, we utilized the widely recognized COVID-19 Radiography Database. The dataset was systematically partitioned to ensure robust evaluation, with the data randomly split into training, testing, and validation sets at a ratio of 7:2:1 (70% for training, 20% for testing, and 10% for validation). All images underwent standard preprocessing steps, including resizing to uniform dimensions and normalization, to standardize the feature scale and ensure the reproducibility of the experimental results.

Let $X \in R^{B \times C \times H \times W}$ denote the input feature map from the preceding convolutional stage, where *B, C, H*, and *W* represent the batch size, number of channels, height, and width, respectively. The fuzzy layer introduces two trainable parameters for each channel $c \in \{1,\ldots,C\}$ the center μ_c (mean) and the width σ_c (standard deviation), which correspond to the threshold voltage (V_{th}) and the subthreshold swing of the hardware device, respectively.

The operation of the layer consists of three steps:

(1) Gaussian membership mapping:

Similar to the device's current modulation, the input features are mapped to a membership degree using a Gaussian function. For a feature value $x_{c,h,w}$ at position (h, w) in channel c, the membership grade $g_{c,h,w}$ is calculated as

$$g_{c,h,w} = exp(-\frac{1}{2}(\frac{x_{c,h,w} - \mu_c}{\sigma_c + \epsilon})^2)$$

where ϵ is a small constant (10^{-4}) to ensure numerical stability. This step acts as a "soft" gate, assigning higher weights to features that fall within the specific "active region" defined by the learned μ_c and σ_c, effectively filtering out background noise and irrelevant feature activations.

(2) Non-linear feature modulation:

The original features are then modulated by their calculated membership grades:

$$X_{modulated} = G \odot X$$

where $\odot$ denotes the element-wise (Hadamard) product. This mechanism suppresses features with low membership (noise) while preserving salient features, mimicking the high on/off ratio modulation of the BP transistor.

(3) Residual Transformation:

To integrate this modulation into the deep network without hindering gradient flow, we employ a residual architecture. The modulated features pass through a lightweight transformation block $f(\cdot)$ consisting of a 3×3 convolution, Batch Normalization, and ReLU activation. The final output *Y* is given by

$$Y = X + \lambda \cdot f(X_{modulated})$$

where λ is a scaling factor (set to 0.1 in our implementation) to stabilize training. This structure allows the network to learn subtle feature refinements adaptively, corresponding to the "fine-tuning" capability of the fuzzy logic hardware.

Supplementary Section 1. Transfer characteristics of the WSe_2 device under different polarization voltages using the same device architecture

To further validate the material selection, we fabricated a control device by replacing BP with WSe_2 under the same device structure. Unlike BP, the WSe_2 transistor shows no evident ambipolar transport behavior, indicating that carrier injection is dominated by a single polarity. This comparison further confirms that BP, with its narrower bandgap, is more suitable for achieving symmetric ambipolar transfer characteristics required for Gaussian-like responses.

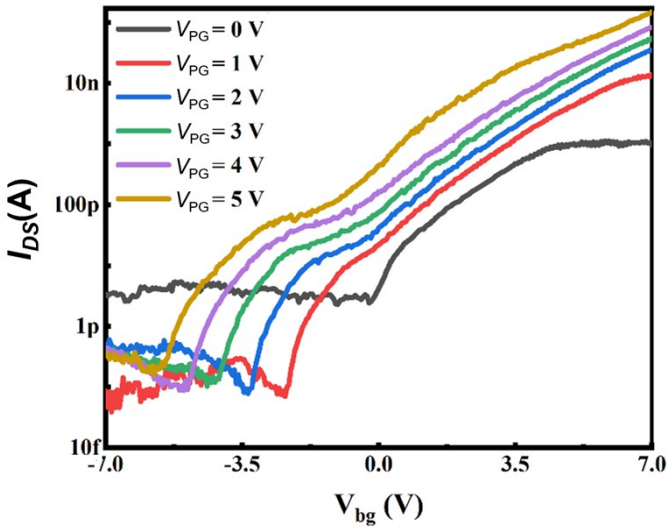

Supplementary Figure S1. Transfer characteristics of the WSe_2 device under different polarization voltages.

Supplementary Section 2. Comparison of electrical characteristics for the BP transistor on a SiO_2 substrate

To verify the universality of the Al_2O_3 encapsulation strategy, we investigated the electrical transport properties of a BP device fabricated on a standard 285 nm SiO_2/Si substrate. The BP channel thickness was approximately 10 nm. Electrical measurements were performed in a vacuum probe station to exclude environmental interference. First, the pristine BP device was characterized while protected by a PMMA layer. We swept the back-gate voltage (V_{bg}) from −40 V to 40 V with a step size of 0.2 V, maintaining a constant source-drain bias (V_{ds}) of 1 V. As illustrated by the black curve in Figure S1, the pristine device exhibited pronounced p-type behavior with an on-state current of approximately 10^{-5} A. Subsequently, after the deposition of the Al_2O_3 encapsulation layer, the device was re-measured under identical bias conditions. The post-doping transfer characteristic (red curve) demonstrates a transition to distinct ambipolar behavior. Specifically, the electron branch (n-type) current increased to 10^{-7} A, while the hole branch (p-type) current decreased to 10^{-6} A. This significant modulation of the threshold voltage and the emergence of electron conduction confirm that the n-type doping effect induced by the fixed positive charges in Al_2O_3 is intrinsic to the interface and independent of the underlying substrate material.

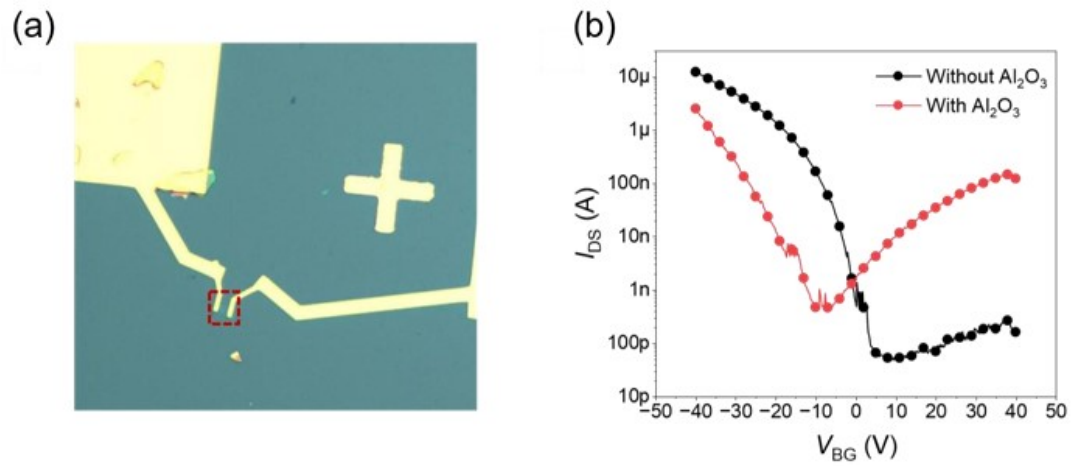

Supplementary Figure S2. Comparison of the BP device on a SiO_2 substrate before and after Al_2O_3 encapsulation. (a) Optical microscope image of the BP device after Al_2O_3 encapsulation. (b) Comparison of electrical characteristics; the black curve represents the pristine BP device without Al_2O_3, and the red curve represents the Al_2O_3-encapsulated BP device.

Supplementary Section 3. The optical-linear response of the BP split-gate architecture

To explore the capability of the split-gate structure for achieving linear response characteristics, a split-gate BP device was fabricated, as illustrated in Supplementary Fig. S3(a). The BP channel is encapsulated by Al_2O_3 and controlled by two independent gates, namely the left gate (LG) and the right gate (RG), which electrostatically modulate the carrier polarity in different regions of the channel. By tuning the gate biases, reconfigurable homojunctions can be formed within the BP channel.

During the measurements, the RG was fixed at 0 V while the device response was modulated by sweeping the LG. The corresponding response characteristics are shown in Supplementary Fig. S3 (b). Owing to the effective junction modulation enabled by the split-gate configuration, the device exhibits a nearly linear response over a wide voltage range. This behavior demonstrates the capability of split-gate BP devices to realize linear response characteristics, which are essential for linear neural network computation.

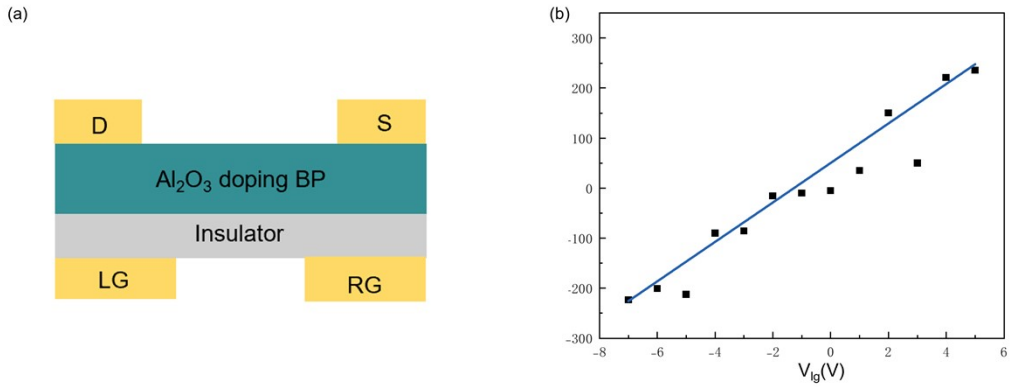

Supplementary Figure S3. (a) Schematic of the split-gate BP device with Al_2O_3 encapsulation. (b) Linear response of the device.

Supplementary Section 4. Visualization of feature enhancement and noise suppression by the fuzzy logic layer

Figure S4 illustrates the evolution of CT imaging features across four distinct pathological conditions. Raw input images are frequently compromised by inherent noise, insufficient contrast, and blurring artifacts, which introduce significant uncertainty into pathological identification. While standard CNN processing effectively enhances high-frequency edge features and outlines major anatomical structures, it often prioritizes coarse feature extraction, leaving subtle tissue textures and fine-grained details insufficiently resolved for precise diagnostic analysis. Upon processing through the fuzzy logic layer, these subtle regions are adaptively modulated; specifically, the nonlinear gain mechanism allows previously ambiguous lesion areas to manifest clearly within the feature maps. This synergistic integration of CNNs with fuzzy logic not only reinforces dominant structural features but also provides critical diagnostic support in regions of high uncertainty, thereby offering enriched, high-confidence reference information for clinical decision-making.

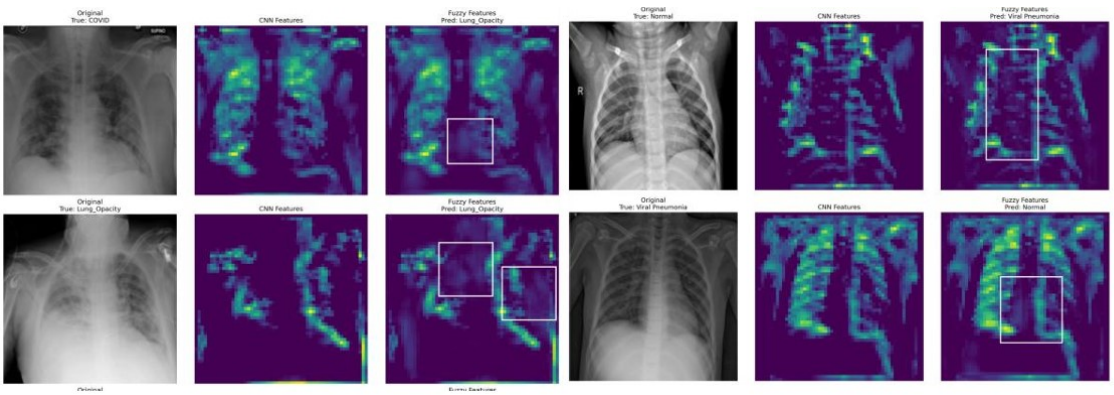

Supplementary Figure S4. Visualization of recognition results at different stages of the fuzzy identification process.

Supplementary Section 5. Extended Validation in Space–Ground Optical Transmission

To further validate the effectiveness of the proposed FEL-CNN for symbol recognition in space-ground optical communication scenarios, we construct a baseline CNN with two convolutional layers and a FEL-CNN with an identical backbone architecture where a Stable-Fuzzy-Layer is inserted after the second convolutional layer. The fuzzy layer employs Gaussian membership functions to adaptively fuzzify feature maps, thereby enhancing robustness against Gaussian blur and noise commonly encountered in optical channels. The dataset is generated through simulation and contains eight modulation classes with 200 samples per class, where random Gaussian blur (kernel size 5–15, standard deviation 1.0–3.0) and additive white Gaussian noise (SNR = 3 dB) are introduced. The validation accuracy and loss curves during training demonstrate that, compared with the conventional CNN, the FEL-CNN achieves higher final recognition accuracy, faster convergence, and improved training stability.

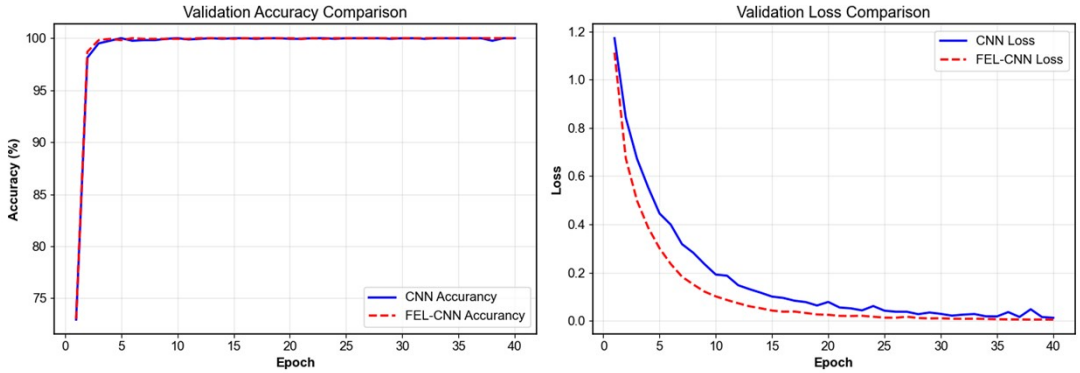

Supplementary Figure S5. Validation accuracy and loss curves of the baseline CNN and the proposed FEL-CNN over 40 epochs. The FEL-CNN shows faster convergence and lower validation loss, indicating improved training stability and robustness due to the fuzzy layer.

References:

(1) Liu, H., Wu, J., Ma, J. et al. A van der Waals interfacial junction transistor for reconfigurable fuzzy logic hardware. Nat. Electron. 2024 7, 876–884. https://doi.org/10.1038/s41928-024-01256-3

(2) Leong, J. F.; Sivan, M.; Pan, J.; Fang, Z.; Li, J.; Xu, Z.; Zhao, S.; Wan, Q.; Zamburg, E.; Thean, A. V.-Y. Opportunities for 2D-Material-Based Multifunctional Devices and Systems in Bioinspired Neural Networks. Small 2025, 21, 2403606, doi:10.1002/smll.202506638.

(3) Huang, Y.; Tan, Y.; Kang, Y.; Ding, W.; Tang, Y.; Jiang, T. All-Optically Triggered In-Sensor Collision Detection and Warning Based on 2D Complementary Material Devices. *Adv. Funct. Mater.* 2024, 34, 2403799, doi: 10.1002/adfm.202402677.

(4) Sun, H.; Chen, P.; Ming, Z.; Zhang, Z.; Tai, Y.; Tian, Y.; Ge, B.; Zhang, Z.; Zhou, P. Ambipolar ohmic contact to silicon for high-performance brain-inspired image sensors. *Nat. Commun.* 2025, 16, 355, doi: 10.1038/s41467-025-63193-9.